

IAC-13-B4.7.2

DESIGN AND ANALYSIS OF DISTRIBUTED NANO-SATELLITE SYSTEMS FOR MULTI-ANGULAR, MULTI-SPECTRAL EARTH OBSERVATION

Sreeja Nag

Massachusetts Institute of Technology, U.S.A., sreeja_n@mit.edu

Distributed Spacecraft Missions can be used to improve science performance in earth remote sensing by increasing the sampling in one or more of five dimensions: spatial, temporal, angular, spectral and radiometric. This paper identifies a gap in the *angular* sampling abilities of traditional monolithic spacecraft and proposes to address it using small satellite clusters in formation flight. The angular performance metric chosen to be Bi-directional Reflectance Distribution Function (BRDF), which describes the directional and spectral variation of reflectance of a surface element at any time instant. Current monolithic spacecraft sensors estimate it by virtue of their large swath (e.g. MODIS, POLDER), multiple forward and aft sensors (e.g. MISR, ATSR) and autonomous manoeuvrability (e.g. CHRIS, SPECTRA). However, their planes of measurement and angular coverage are limited. This study evaluates the technical feasibility of using clusters of nanosatellites in formation flight, each with a VNIR imaging spectrometer, to make multi-spectral reflectance measurements of a ground target, at different zenith and azimuthal angles simultaneously. Feasibility is verified for the following mission critical, inter-dependent modules that need to be customized to fit specific angular and spectral requirements: cluster geometry (and global orbits), guidance, navigation and control systems (GNC), payload, onboard processing and communication. Simulations using an integrated systems engineering and science evaluation tool indicate initial feasibility of all listed subsystems.

I. INTRODUCTION

Distributed Spacecraft Missions (DSMs), or space missions with using multiple spacecraft with a common goal, have been gaining momentum in the last few decades owing to their ability to improve spatial and temporal performance and reduced risk through increased ‘ilities’¹. DSMs are prohibitively expensive unless small spacecraft are used such that many can be developed and deployed at or less than the cost of one. Cost, schedule and risk considerations in monolithic and distributed missions have ushered in an era of small satellites to complement flagship missions in the important field of earth observation and remote sensing². Nanosatellites (<10kg), now also known as the CubeSat class of satellites, are convenient small satellites to demonstrate better and cheaper performance because they have additional advantages of access to a standard CubeSat bus and secondary payload launches³.

This paper identifies multi-angular, multi-spectral⁴ (MA-MS) earth observation as an important remote sensing goal that can be best solved using DSMs. It demonstrates an integrated systems engineering and science valuation tool to design the subsystems in keeping with science traceability, technological constraints and subsystem interdependencies. It evaluates the feasibility of a nanosatellite DSM as the most science-performance efficient method to meet such a goal and proposes a science-optimal baseline design.

I.I. Distributed Spacecraft Missions (DSMs)

DSMs encompass a diverse family of spacecraft configurations. They include homogenous constellations

such as GPS and Iridium, heterogeneous constellations such as the A-Train, close proximity clusters in active formation flight such as the upcoming Proba-3⁵ and fractionated spacecraft where all physical entities share subsystem functions such as System F6⁶. DSMs may have inter-satellite communication links which dictates their relative distance requirements. They may be deployed in a staged fashion⁷, reconfigurable while in orbit and replenished when older satellites cause graceful degradation⁸. This allows for scalability, flexibility and evolvability in the mission and puts less pressure on risks and schedule. Technologies to support DSMs have also seen a great increase: Proximity operations and formation flight⁹⁻¹¹, orbit initialization and scatter maneuvers¹², high data rate communication links¹³, miniaturized thrusters for active control¹⁴ and open-source cluster flight development^{11,15-17}. While on-orbit demonstrations have been few, new technologies and smaller spacecraft show an optimistic future for DSM demonstrations for improved science.

I.II. DSMs for Improved Sampling

In earth science remote sensing, DSMs can be efficient in directly improving sampling in three out of five dimensions of an observed image – *spatial, temporal, angular, spectral and radiometric*.

Spatial resolution of an image can be increased by using multiple satellites in formation flight to synthesise a long baseline aperture as shown for optical interferometry¹⁸ and synthetic aperture radars. This avoids the monolithic need of larger apertures and heavier optics to achieve the same resolution. High

spatial resolutions are important for analysing geophysical phenomena at small spatial scales such as canopy structures in arid regions¹⁹.

While satellites may be deployed on a repeating ground track orbit, global coverage is severely compensated if the repeats are designed to be too frequent. Temporal repeats within a few hours as well as continuous coverage maintenance is important for studying global phenomena with fast temporal variability such as hurricanes, tropical clouds²⁰ and is only possible using constellations of evenly spaced satellites.

Angular sampling implies taking images of the same ground spot at multiple 3D angles of solar incidence and reflection simultaneously. The near-simultaneous measurement requirement deems monoliths insufficient for accurate and dense angular sampling (Figure 1). Monolithic spacecraft have traditionally approximated the angular samples by combining measurements taken over time with forward-aft (e.g. TERRA's MISR²¹) or cross-track swath (e.g. TERRA's MODIS²²) sensors. However, a single satellite can make measurements only along a restrictive plane with respect to the solar phase and most earth observation satellites are even more restricted since they are on sun-synchronous orbits. Further, the angular measurements are separated in time by many minutes along-track or weeks cross-track. In areas of fast changing surface/cloud conditions especially during the melt season/tropical storms, a few days can make a big difference in reflectance.

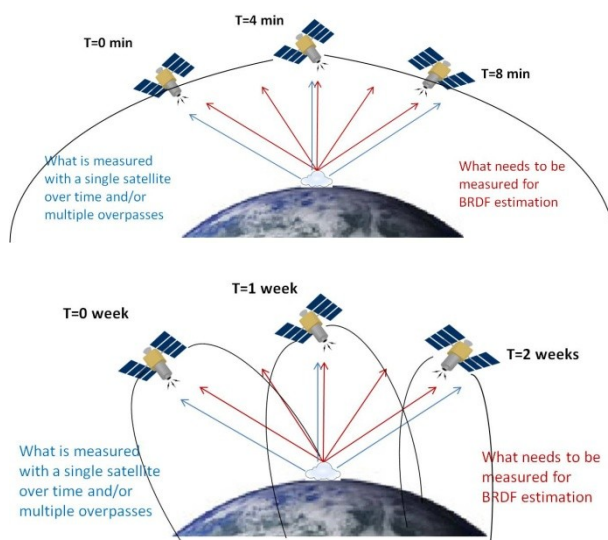


Figure 1: Measurements a single satellite is capable of making, in blue, versus multiple angular sampling measurements in red. ‘T’, ranging over a few minutes for fwd-aft sensors in the top panel or over a few weeks for cross-track sensors in the bottom panel, represents nominal time differences that a LEO satellite takes to make the given measurements.

Spectral resolution can be improved by increasing the wavebands in the payload, however at the cost of spectral range or coverage. Large spectral range can be achieved for many wavebands by using multiple payload spectrometers and corresponding focal plane arrays (FPAs) so that different regions of the spectrum are mapped on different FPAs. However, the telescope is usually common for the entire spectra and the aperture diameter limits the spatial resolution at lower frequencies of the spectrum. Also, since the total imaging time is restricted by the satellite's ground speed, there is a trade-off between the number of spatial pixels (swath) and the number of wavebands (spectral range) that can be imaged²³. DSMs can be used to fractionate the payload (fractionated spacecraft) such that each physical entity images a different part of the spectrum and has customized optics to do so. Lower bands per ‘fraction’ allow more spatial pixels and a larger swath.

Radiometric resolution is indirectly proportionate to the time it takes to readout an image on the FPA and also directly affects image noise. High radiometric sampling limits the number of pixels (i.e. swath and global coverage) and wavebands (i.e. spectral range), that can be imaged²³. If the spectrum is fractionated and global spatial coverage is achieved using constellations, then more radiometric sampling can be achieved without a science cost in a different dimension.

I.III. Metrics for Angular Sampling

This paper will concentrate on proving the utility of DSMs to improve angular sampling in earth observation. The widely accepted metric to quantify the angular dependence of remotely sensed signal is called BRDF or Bidirectional reflectance-distribution function. BRDF of an optically thick body is a property of the surface material and its roughness. It is the ratio of reflected radiance to incident irradiance that depends on 3D geometry of incident and reflected elementary beams²⁴. To name a few, it is used for the derivation of surface albedo²⁵, calculation of radiative forcing²⁶, land cover classification²⁷, cloud detection²⁸, atmospheric corrections, and aerosol optical properties²⁹. Accurate BRDF time series at customized spectra and spatial scales can estimate many biophysical phenomena that are currently wrought with errors. For example, up to 90% of the errors in the computation of atmospheric radiative forcing, which is a key assessor of climate change, is attributed to the lack of good angular description of reflected solar flux³⁰. MODIS albedo retrievals show errors up to 15% due to its angular and spatial under sampling when compared to CAR. Gross Ecosystem Productivity (GEP) estimations, to quantify sinks for anthropogenic CO₂, show uncertainties up to 40% and usage of CHRIS angular data has shown to bring them down to 10%³¹. Accuracy of BRDF

estimation is therefore a representative metric of the ‘goodness’ of all five sampling dimensions discussed previously.

BRDF Science Metrics Current Instruments	Number of angles	Ground Pixel Size in km X km	Revisit Time (any view) in days	Spectral Range	# of spectral bands
¹ MODIS	1	0.25 to 1	~2(16day RGT)	0.4-1.4 μm	36
¹ POLDER	14	6 X 7	~2(16day RGT)	0.42-0.9 μm	9
¹ CERES	1	10 to 20	~2(16day RGT)	0.3-12 μm	3
² MISR	9	0.275 to 1.1	9(16day RGT)	0.44-0.87 μm	4
² ATSR	2	1 to 2	3-4	0.55-12 μm	7
² ASTER	2	0.015 to 0.09	~2(16day RGT)	0.52-11.65 μm	14
³ CHRIS	5-15	0.017 to 0.5	As per command	0.415-1.05 μm	18-63

Table 1: Comparison of current spaceborne mission instruments with BRDF products (rows) in terms of BRDF measurement metrics (columns). Red highlights indicate sparse measurements for BRDF estimation.

Airborne instruments estimate local BRDF very accurately because they are able to fly around a ground spot taking thousands of angular measurements. NASA’s heritage airborne BRDF instrument is called the Cloud Absorption Radiometer²⁹ (CAR), developed at Goddard Space Flight Centre (GSFC), has 14 channels of bandwidth 6-40 nm, makes up to 114600 directional measurements of radiance per channel per aircraft circle at a spatial resolution of 10-270 m²⁹. However, these measurements cannot be scaled up globally or repeated temporally.

Spacecrafts can only approximate BRDF to varying degrees of inaccuracy (Figure 1). Their instruments, as shown in Table 1, estimate BRDF by making multi-angular measurements owing to their large cross track swath¹ (e.g. MODIS²², POLDER³², CERES³³), multiple forward and aft sensors² (e.g. MISR²¹, ATSR³⁴, ASTER³⁵), or autonomous manoeuvrability to point at specific ground targets that they have been commanded to observe³ (e.g. CHRIS³⁶). Other than CHRIS (which does not provide global or repeatable coverage) and POLDER (with very coarse spatial resolution), none of the instruments provide full 3D angular coverage within a short time frame. Some instruments like MISR are also limited in resolution of the solar spectra.

II. RESEARCH METHODS

A possible solution to improving the angular sampling of the BRDF function is the use of a cluster of nanosatellites on a repeating-ground-track orbit³⁷. The cluster can make multi-spectral measurements of a ground spot at multiple 3D angles at the same time as they pass overhead either using narrow field of view (NFOV) instruments in controlled formation flight (Figure 2-left) or wide field of view (WFOV) instruments with overlapping ground spots imaged at different angles (Figure 2-right). The mission will not only need precise relative formation flight but also strict attitude control, orbit maintenance, onboard

processing for the multi-spectral data, inter-satellite calibration and a good communication channel to downlink the collected data. Therefore, there is a need for detailed, quantitative methods to evaluate its feasibility within achievable COTS (Commercial Off-The-Shelf) technologies and costs.

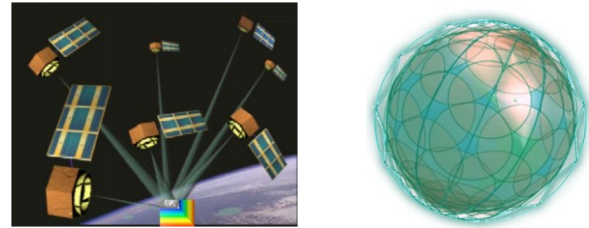


Figure 2: [Left] A DSS making multi-angular, multi-spectral measurements by virtue of pointing its NFOVs at the same ground spot, as it orbits the Earth as a single system (adapted from Leonardo BRDF²⁸). [Right] A DSS making multi-angular, multi-spectral measurements by virtue of their overlapping WFOVs at different angles (from GEOScan³⁸).

II.I. Goals and Objectives

The goal of the overall study is to use a systems engineering approach to evaluate the feasibility of and decide on a baseline architecture for a DSM to estimate BRDF. Specific research questions include: Is it technically feasible for a nanosatellite cluster to optimally sample the angular dimension of the BRDF function better than successful air/space missions over a mission’s lifetime? What changes in the design are required to customize the spatial, spectral and temporal sampling of the function? How can we select the “Pareto Optimal” cluster architecture (maximum science performance at minimum lifecycle cost)? How do these clusters compare with existing monolithic spacecraft in terms of BRDF science achievable traded against mass or cost?

The objectives for *this* paper are restricted to evaluating the technical feasibility of mission critical astrodynamics and spacecraft subsystems, taking into account their inter-dependencies, required to improve angular sampling of the BRDF function compared to existing instruments.

II.II. Measurement Requirements

The mission measurement goals are derived from the science goals and requirements of current, successful spaceborne instruments and airborne instruments. Measurement zenith angles up to 80°, measurement azimuth up to 360°, solar zenith angles up to 80° are required for the full angular spread. The CAR²⁹ instrument standards require a spectral resolution varying between 10-40 nm depending on the region of the spectrum, number of wavebands > 14, spectral range

between 350 and 2300 nm from CAR. The payload can be a spectrometer or a radiometer. A medium spatial resolution of < 400 m is considered as an initial requirement (from MISR), however the approach should allow this to be customizable. The altitude range requirements used are 500 km to 800 km (LEO) because that range corresponds to the most common shared rides available with primary payloads³⁹. If all the nanosatellites are launched as the primary payload itself, then the orbit constraints may be removed. The bus requirements are set to mass < 10 kg, physical dimensions $< 10 \times 20 \times 30$ cm and power < 25 W, to adhere to expected 6U CubeSat standards.

II.III. Systems Engineering Model

To address the research objective, a systems engineering (SE) model integrated with traditional BRDF estimation models (science model) for tradespace exploration and optimization was built as shown in Figure 3. The SE model will contain the following modules as shown in Figure 4 as a design structure matrix (DSM) or an N2 diagram: cluster geometry (and global orbits), guidance, navigation and control systems (GNC), payload, onboard processing, communication and cost. The subsystem modules have been identified as critical for the mission and need special customization. For example, power has been left out because there are no special power requirements over the 6U CubeSat standard. The vertical arrows represent inputs and horizontal arrows outputs from the subsystems.

The SE model will take BRDF measurement requirements and 6U cubesat/nanosatellite bus requirements as inputs (as identified in the previous section), use them as constraints to generate hundreds of cluster architectures and output two types of metrics seen in Figure 4- science performance (e.g. Signal-to-Noise Ratio or SNR) and resource measures (e.g. mass). The model will also allow optimization within the individual modules to maximize metric values.

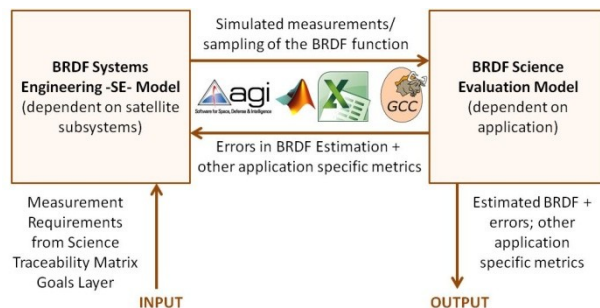


Figure 3: Flow of information between the integrated systems engineering model and the BRDF science evaluation model to quantitatively compare different space architectures with one another in terms of science achievable and to iterate to find the optimal architecture for specific science applications.

As seen in Figure 4, the *cluster geometry module* will check all the closed loop solutions of the modified Hill's equations⁴⁰ that satisfy input constraints or the measurement requirements. Additional inputs may include specific orbit requirements for coverage and revisit or specific application-based geometries (e.g. BRDF for radiative forcing estimation needs quadrature arrays²⁸). The slew rate of payload pointing required for all the geometry solutions will drive the *GNC module* to find required angular momentum and torque capacity of the ADCS system to achieve payload pointing. The GNC sensors and range will constrain the inter-satellite distances in the cluster module through a feedback loop.

The *payload module* will include a full physics-based optimization to find optical requirements based on external (mission or other module) requirements, use them to design dispersive spectrometers that will fit within the 6U payload bay and evaluate their performance. The field of view and spatial resolution provided by the payload will drive the attitude determination and control bits required in the GNC module. The *onboard processing module* takes in the raw images from the payload and position information from the GNC module and performs hyperspectral processing to compress the image. It then accurately registers the image so that it can be overlaid later with processed images from other satellites in the cluster obtained at the same ground spot at different angles.

The *communication module* then transmits the processed images down to the Earth at the next downlink opportunity as a function of the range and elevation to ground station as obtained from GNC. The *cost module* is used to cost every architecture, calculate its complexity and associated risks to trade against the science performance of that architecture.

Science performance is quantified by the SE model's individual output metrics (science metrics in Table 1), estimation uncertainties for specific geo-science applications of BRDF (such as albedo and GPP) and errors from BRDF estimation models using these angular spread as input. The Coupled Surface-Atmosphere Reflectance (CSAR) model and RossThick-LiSparse (RTLS) model⁴¹ along with the SE Model's simulated multi-spectral, multi-angular radiance measurements are used to estimate BRDF and associated errors. To evaluate the payload, radiance will be simulated within the payload module using NASA Langley's Coupled Ocean and Atmosphere Radiative Transfer (COART) Model⁴², which is also used to estimate SNR. These models have been widely used for previous BRDF data products and are ideal for comparing data products from the proposed cluster architectures with existing instruments.

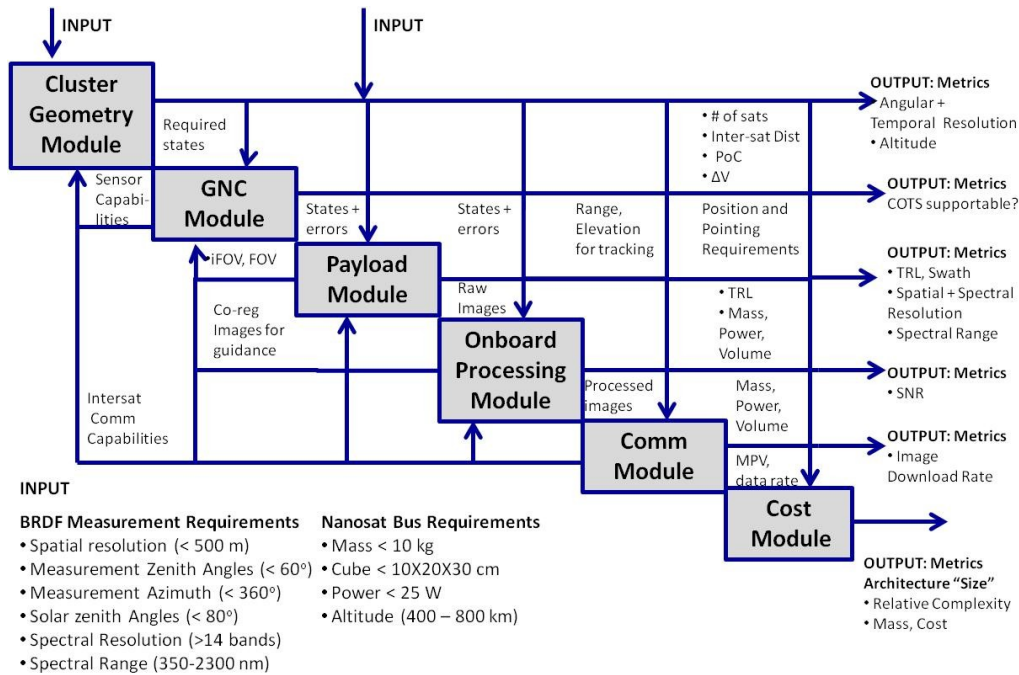


Figure 4: Systems Engineering Model (inside the left hand box of Figure 3) showing the inputs – vertical arrows - from measurement requirements or from other subsystem outputs and outputs – horizontal arrows – to evaluate the eligibility and performance of any selected architecture.

II.IV. Metrics to Determine Feasibility

Many DSM architectures generated by running the SE model for different subsystem variables within the measurement requirements. Technical feasibility of these architectures is determined by the output values shown the right side of Figure 4: Angular, temporal, spatial and spectral resolution, signal to noise ratio (SNR), swath, technology readiness level (TRL) and image downloading rate. Only architectures with values greater than a threshold will be considered for those variables that have strict requirements and for all others, the more the value, the better. Technologies required by the GNC module (e.g. star tracker accuracies) will be checked if COTS supported and if channels for the required data rates can be obtained. Finally, all these performance metrics for all the possible architectures will be traded against corresponding cost and a Pareto front obtained. A baseline mission architecture will be selected from this front and will therefore be Pareto Optimal. In this paper, *only* technical feasibility of the individual subsystems using the variables mentioned will be ascertained. The subsystems are modelled with inter-dependencies, demonstrated in the next section.

III. RESULTS

This section presents the results of the SE model in Figure 4, for the critical, individual subsystems with interdependencies. Only those architectures that satisfy

the requirements are considered and technologies required to make them possible cited.

III.I. Cluster Configurations

The technical feasibility of the DSM's formation flight is assessed in terms of configurations available to achieve BRDF angular spread. Multiple solutions are proposed at three levels of fidelity – Hill's equations, dual spiral equations and global orbit propagation using AGI's STK⁴³. Initial simulations³⁷ have shown that string of pearls (SOP), cross-track scan (CTS) and free orbit ellipse (FOE) geometries for varying phasing parameters cover a large angular and altitude spread. The geometries are numerically corrected to account for curvature of the earth at large intersatellite distances where the Hill's linearization breaks down.

Thousands of configurations were considered for all geometries by varying the number of satellites, number of rings, azimuthal spread on the rings, inter satellite distances, orientation and size of the ellipses and so on and the corresponding view zenith and relative azimuth angle sets for all architectures calculated.

As a case study, reflectance values corresponding to the measurement angles were obtained from a BRDF database collected by the CAR instrument during an Arctic snow campaign. These values, now considered simulated measurements, were then fit on a standard

BRDF model called Ross-Sparse Li-Thick (RLTS) model and model parameters estimated. The model's predicted reflectance values for all 3D angles using the estimated model parameters were compared to the database values and an RMS error obtained. For a system of 13 satellites, the least RMS error (0.0004) was obtained by the cluster configuration shown in Figure 5. This configuration has a chief orbit altitude of 600 km, 13 satellites in 4 rings, ellipse tilted at 21.8 deg with the chief orbit X=0 plane. The nominal view zenith angles when the satellites intersect the chief orbit for the 4 rings are 0, 20, 40, 50, 60 deg. The RMS error is two orders of magnitude better than obtained by the configuration of the MISR instrument with 9 sensors, simulated using the same methods, proving improved BRDF science performance. RMS errors and albedo (calculated by integrated BRDF over all measurement angles) errors decrease as the number of optimally spaced satellites in the cluster increase - Figure 6.

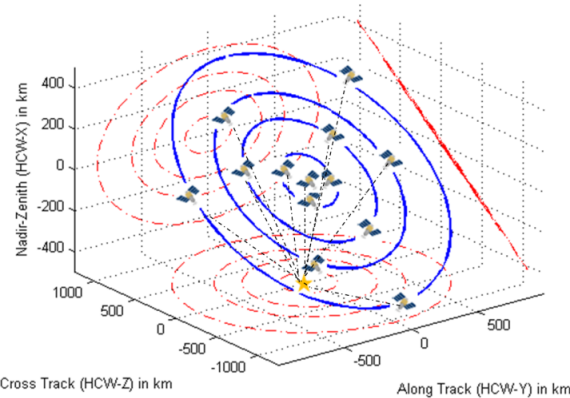


Figure 5: Curvature-corrected Free Orbit Ellipse configuration of a 13-nanosatellite cluster (yellow-blue objects), their trajectories in the HCW frame centered at (0,0,0) (blue lines) and the projections in 3 perpendicular planes (red lines). The orange star represents the target – point on the ground directly below the LVLH origin. The dashed lines indicate the satellite line of sight (LOS) to target.

Simulating the clusters in the Keplerian frame globally shows the variation of angular measurements over mission lifetime, as affected by differential J2 and atmospheric drag. Formation flight can be simulated on STK by fixing a chief orbit for one satellite and perturbing the orbital elements of all other satellites by a small amount. For example, perturbing the true anomaly gives an SOP. Additionally perturbing inclination gives CTS and additionally perturbing eccentricity and/or RAAN gives the FOE.

Using all the dependencies learned from the global STK trade studies, a few candidate clusters with 9 satellites each (to match MISR's sensor numbers) were

simulated in STK to image a specific spot on earth [0, -103.729] at a repeat period of 16 days and compared to the measurement spread of the same ground spot by MISR. Corresponding simulated angular measurements of the target is shown in Figure 7 on a BRDF polar plot.

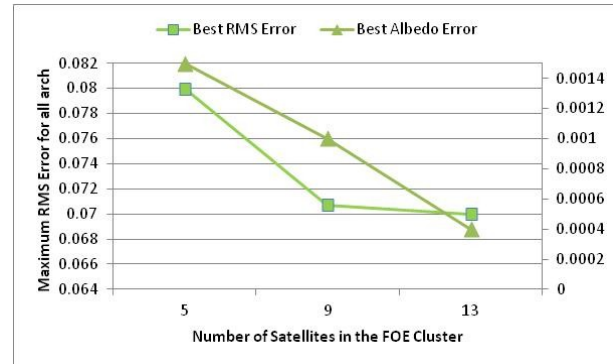


Figure 6: RMS and albedo errors for the most optimal FOE configuration using 5, 9, 13 satellites. Albedo is calculated by integrating BRDF over all measurement angles. The data point corresponding to 13 satellites is obtained by the FOE configuration in Figure 5.

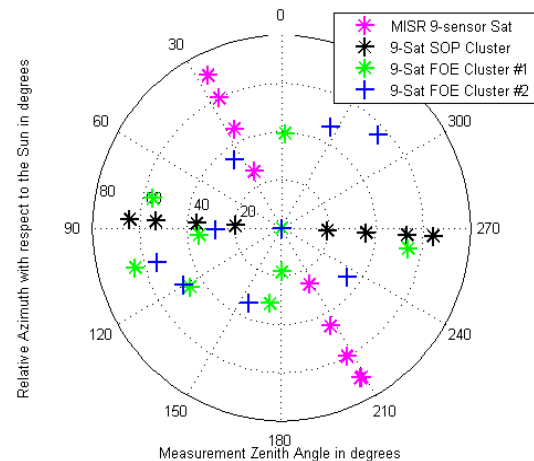


Figure 7: BRDF polar plot for simulated measurements made by three 9-satellite clusters and the MISR instrument using 9 sensors of the same geographic location. STK was used to simulate the measurements and calculate the view zenith (radius) and view relative azimuth (azimuth) angles. The solar zenith angle is ~89°

Three clusters were simulated, one in the SOP configuration (black) with all Keplerian elements except the true anomaly the same and two others in different FOE configurations (blue and green). There was an approximate 60° between the chief orbit of MISR and any of the clusters. Due to MISR's large swath, it has ~1800s of access to the ground spot while the clusters have only 1.4 s in 16 days. Since MISR has fixed sensors, the measurement zenith angles for a direct overpass (plotted in pink) are pre-determined and the relative solar azimuth is the angle between the velocity

and sun vector measured in the satellite HCW $X=0$ plane. These measurements for a single overpass can be replicated by an SOP cluster (plotted in black). The value of clusters is demonstrated in the FOE cluster examples where in a large and diverse azimuthal and zenith spread on the BRDF plot of possible by perturbing the Keplerian elements differentially.

III.II. Global Orbits

While the cluster geometries above demonstrated the technical feasibility of achieving BRDF angular spread using a DSM in formation flight, a global orbit modelling section is required to demonstrate customizable temporal resolution of the images. Being nanosatellites, the swath of the payload is limited (as will be seen in the payload module section) and therefore coverage or repeat period. If the mission demands a temporal imaging within a few hours along with angular coverage, it may be achieved by using many clusters in a constellation or a clustellation at additional cost.

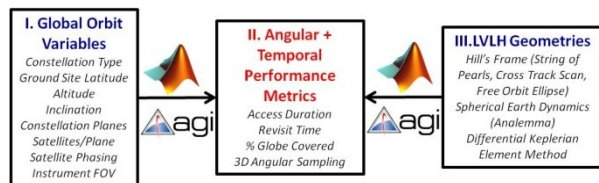


Figure 8: Process Flow Chart for tradespace analysis of DSMs with respect to constellation and cluster orbits. Box I - global design variables, Box III - LVLH design variables, Box II - standard performance metrics.

A trade study demonstrating the dependence of global orbit variables (Box I) on the average revisit time and percentage of globe covered (Box III) was performed, as summarized in Figure 8. Angular coverage (Box II) exclusively depends on the relative geometry of the cluster in the LVLH frame (Box III).

Average revisit time is plotted against six of the orbit variables, taken two at a time, in Figure 9. The baseline values for the others when two are mentioned. The constellation type is set to Walker Constellation. Phasing was not traded because it was observed that it affects revisit periods only negligibly.

This trade study shows that any revisit period and global coverage can be achieved by just increasing the number of clusters in the clustellation. If revisit period is of greater priority than global coverage then a repeat ground track (RGT) orbit can be selected by adjusting orbit altitude and inclination. Figure 9 did not consider RGTs causing the repeat periods to be greater than a day for only one satellite or one cluster (topmost panel).

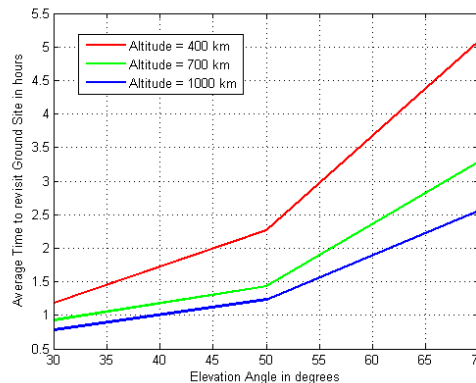
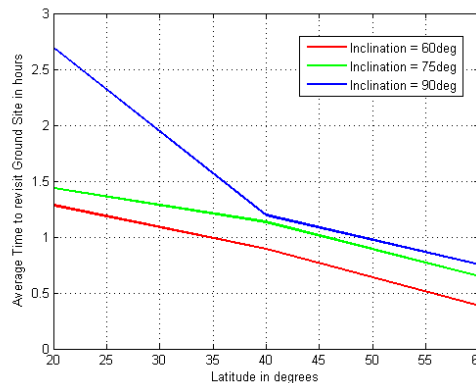
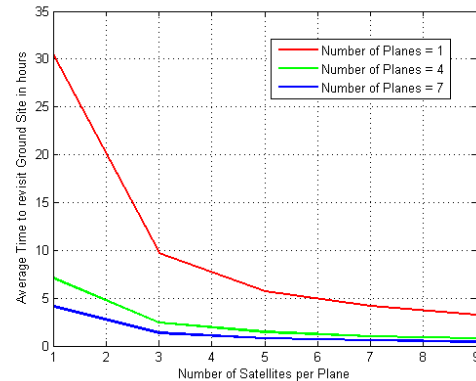


Figure 9: Dependence of average time to revisit the same ground spot on design variables: planes [4], satellites per plane [5], orbit inclination [75deg], latitude of ground spot [20deg], altitude [700km] and minimum elevation angle allowed at ground spot [50deg]. The values in parenthesis indicate the baselines used for the others when pairs of variables are being varied.

III.III. Attitude Determination and Control Systems

The ADCS module is driven by three others: cluster geometry which drives the slewing requirements, payload which drives the determination and control precision and onboard processing which provides the registered images to be used as control points for the satellites' position determination.

Each of the satellites in the cluster will have to *change its pointing direction continuously* to point at the ground spot at reference nadir. Using the ‘most optimal cluster’ shown in Figure 5 as a reference, the required body slew rate and angular accelerations over one orbit for any satellite in each ring was calculated³⁷ (Figure 10). For a 6U cubesat form (which drives moment of inertia), the required angular momentum storage and torque authority from the reaction wheels of the system were easily calculated from the slew rate and acceleration. These values per orbit were found to be within 1-2% of the capacity of standard COTS systems from companies such as Maryland Aerospace (maximum $H=11.8$ mNms, maximum $T=0.625$ nNm for MAI-400) and Blue Canyon Technologies.

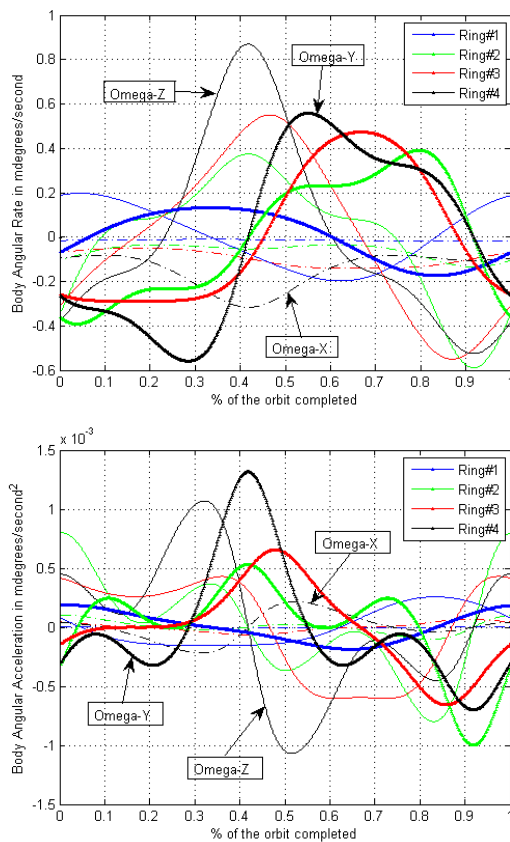


Figure 10: Required body angular rates (top) and angular accelerations (bottom) for a satellite in each ring in the FOE cluster - Figure 5 – to point its payload consistently at the LVLH origin’s nadir point on the ground (orange star). The 3 rings are marked in different colors and ω_x (dashed line), ω_y (thin line), ω_z (thick line) in line types.

The example does not consider drift corrections due to natural disturbances such as differential drag and J_2 , small sat sensor noise and actuation noise from actuation technologies. To account for those, analogous work on precise pointing control with all the above environments in a hardware-in-the-loop (HWIL)

simulation was studied. Tests reviewed included the SPHERES Program, GNC system development via MicroMAS⁴⁴ and ExoplanetSAT⁴⁵ and DSS metric evaluation via the Terrestrial Planet Finder (TPF) program and DARPA System F6, to develop state-of-art algorithms for MAH-EO cluster fight. The reaction wheel stage of ExoplanetSat, both in simulation and HWIL verification on MIT’s spherical air bearing testbed, has shown pointing precision at LEO within 40 arcsec⁴⁵ or 0.011° which meets our pointing requirements (input from the payload module). No additional fine pointing stage is expected to be needed. MicroMAS’s concept of operations (ConOps) have also been tested on the same testbed and the air bearing was able to closely track the commanded angular orientation⁴⁶, verifying the existing HWIL control simulation.

The guidance algorithms for the DSM cluster to measure BRDF will follow the ConOps shown in Figure 11. For the SE model, simulated position and attitude data for cubesats are used and integrates it with the estimator and controller modules (TRL 5) from ExoplanetSat or MicroMAS. The guidance algorithms leverage hyperspectral image processing algorithms from NASA Goddard Spaceflight Centre (GSFC) which has developed a generalized onboard processing module for the same called SpaceCube. Preliminary image co-registration can be done onboard and used to initialize and ensure co-pointing of all the payloads in the cluster. Future work, not required for concept validation, includes testing these GNC algorithms on the high fidelity models of software, actuators, satellite dynamics and space environment that include natural disturbances, processing time, control bandwidths, actuator and sensor error propagations, latency, discretization, quantization and saturation.

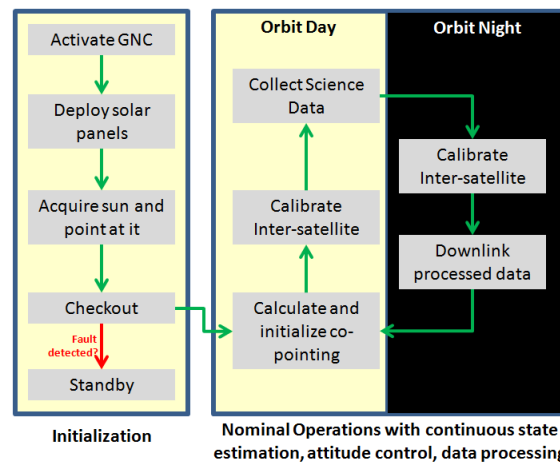


Figure 11: Baseline concept of operations for GNC mode transition for the cluster

III.IV. Spectrometer Payload

DSS can make multi-spectral measurements of a ground spot at multiple 3D angles at the same time as they pass overhead either using NFOV instruments in controlled formation flight (Figure 2-left) or WFOV instruments with overlapping ground spots imaged at different angles flight (Figure 2-right). Small VNIR spectrometers are required as payload on the nanosatellites, customized to sample the BRDF function as required.

The pointing requirements for a mission with NFOV instruments are relatively strict because all the satellites have to point their NFOV payload toward the same ground spot at the same time for the multi-angle image to be correctly registered. If push broom sensors are used, only a single row of pixels will be available in the zenith angular direction and an error equal to the instantaneous field of view (iFOV) would lead to the loss of one angular measurement. For example, if the iFOV is 0.1° , then a satellite's zenith error of 0.1° will cause that satellite to miss the common ground target. This pointing risk may be avoided by the use of hyperspectral snapshot imaging (HSI) which produces 2D spatial images with a single exposure at selected and numerous wavelength bands. HSI is also required if constellations of WFOV satellites are flown such that multi-angle images of any ground spot are generated by co-registering the 3D images from all the satellites in view of the spot because circular or rectangular spots increase the area and instances of overlap. The WFOV approach is a constellation approach to the POLDER instrument and coarsens the spatial resolution of the measurements. Small hyperspectral snapshot imagers for nanosatellites have never been developed, calling for a systems-based approach in designing them and evaluating their feasibility.

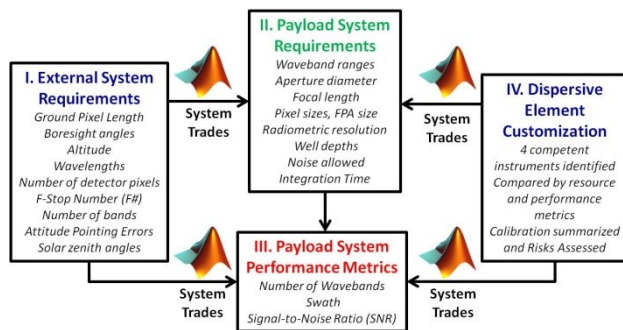


Figure 12: Summary of the modeling approach to design and evaluate hyperspectral snapshot imagers for nanosatellite clusters performing multi-angular earth observation. The model allows tradespace analysis of the spectrometer payload on the satellites in the DSM cluster to map the effect of changing external requirements (Box I) and available dispersive technologies (Box IV) on the optical system (Box II) and performance metrics (Box III)

A system tradespace exploration model²³ is used to estimate the dependence of the payload system requirements (Box II in Figure 12) and the system performance metrics (Box III) on external system requirements (Box I) and on the dispersive element design (Box IV) as seen in Figure 12. The external system requirements are obtained from either BRDF science requirements derived from heritage airborne missions²⁹ (e.g. wavelengths, number of bands, ground pixel length), from the cluster geometry model (e.g. altitude, boresight angles) or nanosatellite technology capabilities (e.g. F#, attitude pointing errors). Four dispersive element types have been proposed along with a CCD array of Silicone and InGaAs diodes as the detectors for snapshot imaging. The dispersers - waveguide spectrometers⁴⁷ (WG), Acousto-optic tunable filters (AOTF)⁴⁸⁻⁵⁰, integral field spectrograph (IFS)⁵¹ and electronically actuated Fabry-Perot Interferometers^{52,53} (FPI) - are compared to each other not only in terms of standalone performance and resources but also on their influence on payload performance metrics. The system trades provide acceptable ranges of payload system requirements which are then used to design a miniaturized spectrometer that fits inside a nanosat bus. The performance metrics provide simple numbers to compare the different payload architectures.

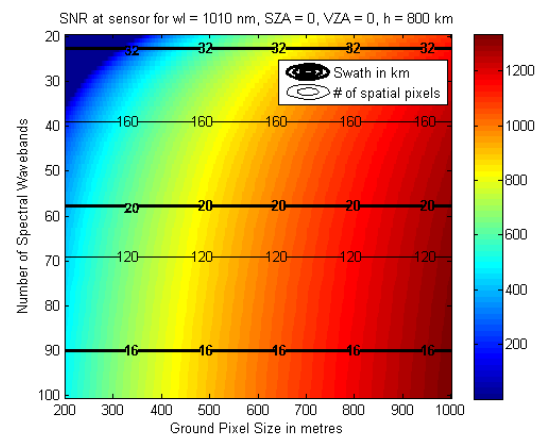


Figure 13: Simulated signal-to-noise ratios (SNR) for Waveguide Spectrometers (left) as a function of spectral wavebands and ground resolution required to be imaged for a nadir looking satellite at 500 km, wavelength of 1010 nm and solar incidence at noon. The contours represent the achievable swath (thick black) and the effective number of spatial pixels available on the FPA (thin black), which is calculated dynamically to maximize swath while allowing at least 5% integration time for a given scenario.

The payload simulation²³ furnish a baseline design for the optical spectrometer that is achievable in a nanosat. The optics required are: aperture diameter of 7 cm, focal length of 10.5 cm, FPA pixel size of 20 μm

and 1000X1000 pixels. Qualitative evaluation favoured AOTFs as the dispersers primarily because of their light weight, small size and flight heritage (TRL>6). However, quantitative analysis showed that WG spectrometers perform better in terms of achievable swath (10-90 km) and SNR (>100) for the same number of imaged wavebands. The different trade-offs between spatial range or swath and spectral range for the waveguide spectrometers (WG) have been clearly quantified in Figure 13 for different wavenumbers and ground resolutions. Increase of SNR with wavebands sounds counter-intuitive but is observed because more wavebands allow lesser FPA space for spatial imaging. This decreases the readout time required after image exposure and increases available integration time, therefore SNR. AOTFs and FPIs (alike), being tunable filters, have the advantage of discontinuous spectral imaging and therefore can outperform WGs if only a few wavebands are needed or the atmospheric absorption bands need to be avoided. The better choice ultimately depends on the geosciences application within multi-angle imaging and the priorities of the listed metrics.

Calibration²³ of the spectrometer will be required both pre-flight in the laboratory to validate the spectrometers and also periodically in-flight to cross-calibrate the spectrometers across the entire cluster. *Pre-flight calibration* is best achieved using integrating spheres available within Goddard's airborne BRDF test facility⁵⁴. *In-flight calibration* is more challenging especially in a small satellite with mass and power constraints. Feasible options include white diffuser plates to reflect sunlight to the spectrometer as in VIIRS⁵⁵ and SELENE⁵⁶, lunar calibration by staring at the moon as in the SEVO payload in the O/OREOS spacecraft⁵⁷ and vicarious calibration using ground control points of well known radiance at the BRDF angles and wavelengths such as the New Mexico or the Sahara desert.

III.V. Communication

A cluster of nanosatellites collecting multi-spectral or even hyperspectral reflectance measurements with reasonable radiometric precision will generate a lot of data compared to typical, heritage nanosatellite missions. Using the payload baseline in the previous section, images at 16-bit resolution are collected only during orbit-day (60-70% of the orbit) for 86 wavebands at a 350 m spatial resolution imaged on a 1000X1000 FPA of a WG spectrometer. This translates to 1.14 TB of data by one satellite in one orbit, all of which needs to be downloaded to save hard disc space on the nanosatellite. Assuming that onboard processing can compress it 6:1 times (demonstrated in the next section) also entails transmitting 191 GB of data. If the baseline

cluster with 13 satellites in Figure 5 were considered, the entire DSM generates 2.48 TB of data every orbit.

Since an average ground station allows a 10 minute window for downlink, we would either need a 4 GBps downlink to transmit all the data down in one go, entailing optical/laser communication, or identify hundreds of ground stations if an S-band downlink is to be used. Note that the numbers have not considered any miss flexibility; allowing a miss margin doubles the required data rate.

Laser communication links greater than 10 GBps have been demonstrated from LEO to ground⁵⁸ and recent SBIRs are funding building the same within 1 kg. NASA Jet Propulsion Laboratory has also shown a 2-wy laser link using 10–25mW, 819nm single-mode communication lasers that served both for communications and fine tracking⁵⁹. Beam divergences exiting the telescope were on the order of 1–2mrad for both beams, which is easily achievable using the ADCS systems already available on the nanosatellite. Bit-error rates nominally were less than 10^{-5} except during dropouts. Downlink can be performed at night when there is little risk of noise and scintillation, especially since the cluster is not in operations mode outside the solar spectrum. Optical communication thus provides an optimistic option to retrieve data from the nanosatellite clusters.

III.VI. Onboard Processing Module

The onboard processing unit will take raw images from the payload module, process them for the communication downlink and also transfer them to GNC module as guidance information. A standardized COTS unit which fits the subsystem interdependencies and requirements in Figure 4 has been identified as NASA GSFC's SpaceCube Mini - an onboard, modular processing unit. The design has been built off the GSFC expertise in designing the legacy SpaceCube 1 that flew on the Hubble Servicing Mission and the ISS MISSE7 experiment⁶⁰. It physically conforms to the volume requirements of a standard 1U (10cm x 10cm x 10cm) Cubesat and incorporates the Xilinx Virtex-5, the latest in high speed, high density, and with the SIRF variant, radiation tolerant FPGA design. Built in peripherals will include 512Mx16 of SDRAM, 96 gigabits of FLASH memory, a radiation hard Aeroflex FPGA (as a watchdog, configuration manager, and scrubber), a 12 bit analog to digital converter, and local power regulation.

The GSFC SpaceCube MINI design also includes one expansion slot to add in an optional user I/O card, thus making it easily adaptable to integrate with the developed GNC software at MIT and any other mission unique I/O software. SpaceCube is being used within the Intelligent Payload Experiment (IPEX), a CubeSat that will launch in October 2013 to validate

autonomous processing and product generation for the Hyperspectral Infra-red Imager (HyspIRI) mission concept⁶¹. It has thus demonstrated high fidelity operations models and hyperspectral image processing, both of which are required for BRDF DSM. SpaceCube 2.0's SAR Nadir Altimetry application has shown a 6:1 reduction in downlink data by moving first stage ground operations onboard, thus useful to make our cluster science data manageable

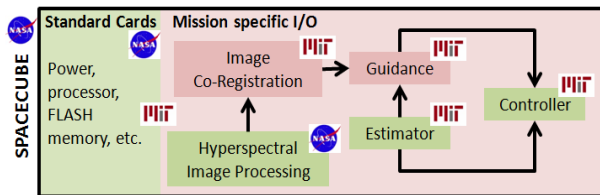


Figure 14: Proposed integrated onboard processing unit for cluster GNC and hyperspectral image processing.
Green: exists, Red: To be developed and integrated

The communication module demonstrated that the acquired data by the cluster is already pretty large for cubesat technologies. This shows a need for significant onboard data processing to reduce the amount of data for downlink, if one wants to use the S-band, and is met using SpaceCube Mini.

Onboard processing is very tightly coupled with GNC. GNC and hyperspectral image processing algorithms will be integrated into the onboard processing unit, customized for CubeSats as summarized in Figure 14. The green sections indicate existing capabilities that will be leveraged and the red sections indicate development required during the build phase of this mission. Each individual section and the interface integrations have been tagged with logos to demonstrate the expected prime contributor, given that GSFC owns SpaceCube while MIT owns the DSM algorithms. The integrated product will be scale-able to clusters, fractionated spacecraft and other DSS and will allow for customization in terms of functionality, autonomy, number of spacecrafts, satellite size, etc.

III.VII. Cost Module

The cost module is currently the least developed in the SE model because of little available literature on both nanosatellite as well as DSM costing. The cost model has been designed to use the Small Satellite cost model to calculate the cost of the monolithic spacecraft bus⁶² (recurring, non-recurring, operations and wrap factors for mass<500 kg). Instrument costs have been estimated using the NASA Instrument Cost Model (NICM)⁶². JHU Applied Physics Lab's costing methods⁶³ (as demonstrated in costing the GEOScan mission³⁸) are used to calculate the cost for producing multiples of the same spacecraft. The cost copy factors, based on historical data, have ranged from 45% for 1

copy to 20% for 5 copies for instruments and 23-54% for the different subsystems with 16% standard deviation. These numbers are used to calculate a learning curve ($b = 0.662$) which is then extrapolated to similar number of multiple spacecrafts. Testing, assurance, systems engineering and other wrapper, operations costs are estimated using the NASA Cost Handbook from cost estimating relationships (CERs)⁶². A simple simulation is used to demonstrate the decrease if marginal costs of building multiple spacecrafts, results seen in Figure 15. The flat curves are attributed to the "fast" learning process ($b=0.662$) derived from APL's studies. Different weights of spacecrafts have been shown to represent the different classes of satellites – nano, micro, mini and large. 20 kg was the minimum weight used because NASA models have yet to confirm CERs for lighter spacecrafts. The increasing costs in Figure 15 can be correlated with the decreasing science errors or increasing science value in Figure 6 to make a systems based decision about how many spacecrafts to fund in a specific science mission.

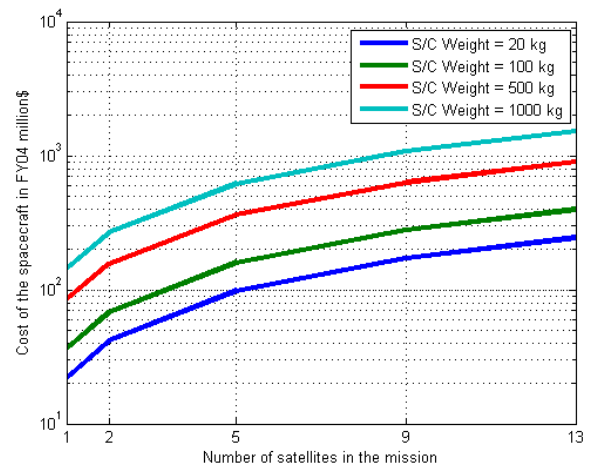


Figure 15: Simulated Mission cost over 2 years for varying total weights and number of identical spacecrafts using parametric CERs and cost copy factors

The cost model will also quantify complexity and risk of the DSM, especially because it is a very new approach. Several studies done by the Aerospace Corporation have demonstrated that complexity is very closely related to cost and that missions that fail or are impaired are mainly those whose cost was too low compared to their complexity^{64,65}. The proposed SE model will have component complexity metrics as a function of the technical uncertainties of the components⁶⁶ (e.g. TRL), structural complexity metrics to capture the dependencies between the modules and therefore emergence behaviours⁶⁷ and dynamic complexity⁶⁷ metrics to represent operational complexity during different mission stages (e.g. Figure 11).

Risk is quantified using the Monte Carlo methods by using probabilistic variables as inputs into the SE model and assessing the probabilistic distribution of the outputs in comparison to the requirements.

IV. FUTURE WORK

The SE model is not entirely ready for a full Pareto front optimization between science performance and cost of the available architectures. Since this paper concentrates on only the technical feasibility of the subsystems, cost analysis has been discussed only briefly. A large section of work on risk and complexity analysis as well as operations cost is yet to be performed before Pareto optimality against performance can be studied.

The presented work is a very quantitative pre-Phase A level study on DSMs for BRDF sampling. As the subsystem models improve, through Phase A and B, greater details in other subsystems that have not been included now can be added. For example, a detailed lifecycle analysis of the cluster evolution due to J2 and atmospheric drag will from the requirements for the propulsion module in the nanosatellites. Currently, the goal is to use electrospray thrusters that will continuously correct for differential forces that try to

break the cluster geometry. Electrospray propulsion is currently being tested in the laboratory at MIT¹⁴ and will take a few years to be flight ready, however are very light and demonstrably perfect for cubesats⁶⁸.

V. CONCLUSIONS

This paper identifies an important gap in the sampling abilities of earth observation missions – that of angular sampling. It proposes the use of nanosatellite clusters in formation flight to fill this gap and demonstrates technical feasibility of the concept using a comprehensive systems engineering model coupled with a science evaluation model. The optimal designs identified show greater angular coverage with lesser BRDF errors than existing missions and their critical subsystems are shown to be COTS supportable.

VI. ACKNOWLEDGMENTS

The author is grateful to Prof. Olivier de Weck and Prof. Kerri Cahoy at MIT and Dr. Charles Gatebe and Dr. Warren Wiscombe at NASA GSFC for very useful discussions on the topics presented in this paper. She also acknowledges the Schlumberger Faculty for the Future Fellowship for financial support to fund this research and her travel to IAC 2013 to present it.

-
1. De Weck, O. L., Roos, D., Magee, C. L. & Charles, M. *Engineering Systems: Meeting Human Needs in a Complex Technological World*. (Mit Pr, 2011).
 2. Kramer, H. J. & Cracknell, A. P. An overview of small satellites in remote sensing*. *Int. J. Remote Sens.* **29**, 4285–4337 (2008).
 3. Skrobot, G. & Coelho, R. ELaNa – Educational Launch of Nanosatellite: Providing Routine RideShare Opportunities. *AIAAUSU Conf. Small Satell.* (2012).
 4. Chopping, M. Terrestrial applications of multiangle remote sensing. *Adv. Land Remote Sens. Syst. Model. Inversion Appl.* 95–114 (2008).
 5. Proba Mission Page on the European Space Agency website.
 6. O'Neill, M. G., Yue, H., Nag, S., Grogan, P. & de Weck, O. Comparing and Optimizing the DARPA System F6 Program Value-Centric Design Methodologies. in *Proc. AIAA Space Conf.* (2010).
 7. De Weck, O. L., Neufville, R. D. & Chaize, M. Staged deployment of communications satellite constellations in low earth orbit. *J. Aerosp. Comput. Inf. Commun.* **1**, 119–136 (2004).
 8. Wertz, J. R. *Orbit & Constellation Design & Management, second printing ed. El Segundo*. (California: Microcosm Press, 2009).
 9. Alvar Saenz-Otero. Design Principles for the Development of Space Technology Maturation Laboratories Aboard the International Space Station. (2005).
 10. Enright, J., Hilstad, M., Saenz-Otero, A. & Miller, D. The SPHERES Guest Scientist Program: collaborative science on the ISS. in *Aerosp. Conf. 2004 Proc. 2004 IEEE* **1**, 46 Vol.1 (2004).
 11. Nag, S. Collaborative competition for crowdsourcing spaceflight software and STEM education using SPHERES Zero Robotics. (2012). at <<http://dspace.mit.edu/handle/1721.1/78499>>
 12. Nag, S. & Summerer, L. Behaviour based, autonomous and distributed scatter manoeuvres for satellite swarms. *Acta Astronaut.* **82**, 95–109 (2013).
 13. Nag, S., Gomez, E., Feller, S., Gibbs, J. & Hoffman, J. Laser communication system design for the Google Lunar X-Prize. in *Aerosp. Conf. 2011 IEEE* 1–20 (2011). doi:10.1109/AERO.2011.5747344
 14. P. Lozano, D. Courtney. On the development of high specific impulse electric propulsion thrusters for small satellites. in *Proc. Symp. Small Satell. Syst. Serv.* (2010).

15. Nag, S., Hoffman, J. A. & de Weck, O. L. Collaborative and Educational Crowdsourcing of Spaceflight Software using SPHERES Zero Robotics. *Int. J. Space Technol. Manag. Innov. IJSTMI* **2**, 1–23 (2012).
16. Nag, S., Katz, J. G. & Saenz-Otero, A. Collaborative gaming and competition for CS-STEM education using SPHERES Zero Robotics. *Acta Astronaut.* **83**, 145–174 (2013).
17. Nag, S., Heffan, I., Saenz-Otero, A. & Lydon, M. SPHERES Zero Robotics software development: Lessons on crowdsourcing and collaborative competition. in *Aerosp. Conf. 2012 IEEE* 1–17 (2012). at <http://ieeexplore.ieee.org/xpls/abs_all.jsp?arnumber=6187452>
18. Kong, E. M. C. & Miller, D. W. Optimal spacecraft reorientation for earth orbiting clusters: applications to Techsat 21. *Acta Astronaut.* **53**, 863–877 (2003).
19. Chopping, M. *et al.* Remote sensing of woody shrub cover in desert grasslands using MISR with a geometric-optical canopy reflectance model. *Remote Sens. Environ.* **112**, 19–34 (2008).
20. Ruf, C. *et al.* The NASA EV-2 Cyclone Global Navigation Satellite System (CYGNSS) Mission. in *Aerosp. Conf. 2013 IEEE* 1–7 (2013). at <http://ieeexplore.ieee.org/xpls/abs_all.jsp?arnumber=6497202>
21. Diner, D. J. *et al.* Multi-angle Imaging SpectroRadiometer (MISR) instrument description and experiment overview. *Geosci. Remote Sens. IEEE Trans.* **36**, 1072–1087 (1998).
22. Xiong, X. *et al.* Terra and Aqua MODIS Design, Radiometry, and Geometry in Support of Land Remote Sensing. *Land Remote Sens. Glob. Environ. Change* 133–164 (2011).
23. Nag, S. *et al.* Evaluation of Hyperspectral Snapshot Imagers onboard Nanosatellite Clusters for Multi-Angular Remote Sensing. in *Proc. AIAA Space Conf.* (2013).
24. Nicodemus, F. E. *Geometrical considerations and nomenclature for reflectance*. **160**, (US Department of Commerce, National Bureau of Standards Washington, D. C, 1977).
25. Lyapustin, A. *et al.* Analysis of snow bidirectional reflectance from ARCTAS Spring-2008 Campaign. *Atmos Chem Phys* **10**, 4359–4375 (2010).
26. Liang, S. *Advances in land remote sensing: System, modelling, inversion and application*. (Springer, 2008).
27. Privette, J. L., Eck, T. F. & Deering, D. W. Estimating spectral albedo and nadir reflectance through inversion of simple BRDF models with AVHRR/MODIS-like data. *J. Geophys. Res.* **102**, 29529–29 (1997).
28. Esper, J., Neeck, S., Wiscombe, W., Ryschkewitsch, M. & Andary, J. Leonardo-BRDF: A New Generation Satellite Constellation. (2000). at <<http://ntrs.nasa.gov/search.jsp?R=20000105058>>
29. Gatebe, C. K. Airborne spectral measurements of surface–atmosphere anisotropy for several surfaces and ecosystems over southern Africa. *J. Geophys. Res.* **108**, (2003).
30. Wielicki, B. A. & Harrison, E. F. Mission to planet Earth: Role of clouds and radiation in climate. *Bull. Am. Meteorol. Soc.* **76**, (1995).
31. Hilker, T. *et al.* Inferring terrestrial photosynthetic light use efficiency of temperate ecosystems from space. *J. Geophys. Res. Biogeosciences* **116**, n/a–n/a (2011).
32. Deschamps, P. Y. *et al.* The POLDER mission: Instrument characteristics and scientific objectives. *Geosci. Remote Sens. IEEE Trans.* **32**, 598–615 (1994).
33. Wielicki, B. A. *et al.* Clouds and the Earth’s Radiant Energy System (CERES): An earth observing system experiment. *Bull. Am. Meteorol. Soc.* **77**, 853–868 (1996).
34. Godsalve, C. Bi-directional reflectance sampling by ATSR-2: a combined orbit and scan model. *Remote Sens.* **16**, 269–300 (1995).
35. Abrams, M. The Advanced Spaceborne Thermal Emission and Reflection Radiometer (ASTER): data products for the high spatial resolution imager on NASA’s Terra platform. *Int. J. Remote Sens.* **21**, 847–859 (2000).
36. Barducci, A., Guzzi, D., Marcoionni, P. & Pippi, I. CHRIS-Proba performance evaluation: signal-to-noise ratio, instrument efficiency and data quality from acquisitions over San Rossore (Italy) test site. in *Proc. 3-Rd ESA CHRISProba Work. Italy* (2005).
37. Nag, S. Design of Nano-satellite Cluster Formations for Bi-Directional Reflectance Distribution Function (BRDF) Estimations. *AIAAUSU Conf. Small Satell.* (2013).
38. Dyrud, L. *et al.* GEOScan: A global, real-time geoscience facility. in *Aerosp. Conf. 2013 IEEE* 1–13 (2013).
39. Marinan, A., Nicholas, A. & Cahoy, K. Ad hoc CubeSat constellations: Secondary launch coverage and distribution. in *2013 IEEE Aerosp. Conf.* 1–15 (2013). doi:10.1109/AERO.2013.6497174
40. W. H. Clohessy, R.S. Wiltshire. Terminal Guidance System for Satellite Rendezvous. *J. Aerosp. Sci.* **27**, 653–658 (1960).
41. Roman, M. O. *et al.* Use of In Situ and Airborne Multiangle Data to Assess MODIS- and Landsat-based Estimates of Surface Albedo. (2012). at <<http://ntrs.nasa.gov/search.jsp?R=20120009500>>
42. Jin, Z., Charlock, T. P., Rutledge, K., Stamnes, K. & Wang, Y. Analytical solution of radiative transfer in the coupled atmosphere-ocean system with a rough surface. *Appl. Opt.* **45**, 7443–7455 (2006).

43. Analytical Graphics, Inc. Satellite Tool Kit. (2013). at <<http://www.agi.com/products/stk/>>
44. William Blackwell (1), Kerri Cahoy (2), David Miller (2), Idahosa Osaretin (1), and Annie Marinan (2). Nanosatellite for Earth Environmental Monitoring: The MICROMAS Project. in 2012.B.2.4 Nanosatellite for Earth Environmental Monitoring, (2012).
45. Pong, C. M. *et al.* One-Arcsecond Line-of-Sight Pointing Control on Exoplanetsat, a Three-Unit CubeSat. *Adv. Astronaut. Sci.* **141**, 147–166 (2011).
46. Crowell, C. W. Development and analysis of a small satellite attitude determination and control system testbed. (2011). at <<http://dspace.mit.edu/handle/1721.1/67177>>
47. Cheben, P. *Wavelength dispersive planar waveguide devices: echelle and arrayed waveguide gratings*. **5**, (chapter, 2007).
48. Georgiev, G., Glenar, D. A. & Hillman, J. J. Spectral characterization of acousto-optic filters used in imaging spectroscopy. *Appl. Opt.* **41**, 209–217 (2002).
49. Glenar, D. A., Hillman, J. J., Saif, B. & Bergstralh, J. Acousto-optic imaging spectropolarimetry for remote sensing. *Appl. Opt.* **33**, 7412–7424 (1994).
50. Hillman, J., Glenar, D., Kuehn, D. M. & Chanover, N. J. Compact Imaging Spectrometers using Acousto-Optic Tunable Filters. *Wkly. News Maganize Sci.* **155**, 26–30 (1999).
51. Bacon, R. *et al.* 3D spectrography at high spatial resolution. I. Concept and realization of the integral field spectrograph TIGER. *Astron. Astrophys. Suppl. Ser.* **113**, 347 (1995).
52. Saari, H. *et al.* Novel miniaturized hyperspectral sensor for UAV and space applications. in *SPIE Eur. Remote Sens.* 74741M–74741M (2009). at <<http://proceedings.spiedigitallibrary.org/proceeding.aspx?articleid=1341656>>
53. Mannila, R., Nasila, A., Praks, J., Saari, H. & Antila, J. Miniaturized spectral imager for Aalto-1 nanosatellite. in 817628–817628–8 (2011). doi:10.1117/12.897999
54. Gatebe, C. K., Butler, J. J., Cooper, J. W., Kowalewski, M. & King, M. D. Characterization of errors in the use of integrating-sphere systems in the calibration of scanning radiometers. *Appl. Opt.* **46**, 7640–7651 (2007).
55. Butler, J. J. *et al.* An overview of Suomi NPP VIIRS calibration maneuvers. in *SPIE Opt. Eng. Appl.* 85101J–85101J–13 (International Society for Optics and Photonics, 2012).
56. Ohtake, M. *et al.* Performance and scientific objectives of the SELENE (KAGUYA) Multiband Imager. *Earth Planets Space EPS* **60**, 257 (2008).
57. Minelli, G., Ricco, A. & Kitts, C. O. O/oreos nanosatellite: A multi-payload technology demonstration. in *Proc. 24th Annu. AIAAUSU Conf. Small Satell.* (2010).
58. Hemmati, H. *Deep space optical communications*. **11**, (Wiley. com, 2006).
59. Wright, M. W. W., Wilson, K. E., Kovalik, J. K., Biswas, A. & Roberts, W. T. R. A bidirectional low Earth orbit-to-ground optical link experiment. *SPIE Newsroom* (2011). doi:10.1117/2.1201109.003826
60. Lin, M., Flatley, T., Geist, A. & Petrick, D. NASA GSFC Development of the SpaceCube MINI. (2011).
61. Chien, S. *et al.* Onboard processing and autonomous operations on the IPEX Cubesat. in *4th Annu. Gov. Forum CubeSats GFC Greenbelt Md. April 16 2012* (2012). at <<http://trs-new.jpl.nasa.gov/dspace/handle/2014/42581>>
62. 65 Authors from the Astronautics Community. *Space Mission Engineering: The New SMAD*. (Microcosm Press, 2011).
63. Whitley, S., Hahn, M. & Powers, N. The Incremental Cost of One or More Copies—Quantifying Efficiencies from Building Spacecraft and Instrument Constellations. in *AIAAUSU Conf. Small Satell.* **52**, 31 (2013).
64. Bearden, D., Cowdin, M. & Yoshida, J. Evolution of complexity and cost for Planetary Missions throughout the development lifecycle. in *Aerosp. Conf. 2012 IEEE* 1–12 (2012). at
65. Bearden, D. A. A complexity-based risk assessment of low-cost planetary missions: when is a mission too fast and too cheap? *Acta Astronaut.* **52**, 371–379 (2003).
66. Murray, B. T. *et al.* *META II Complex Systems Design and Analysis (CODA)*. (DTIC Document, 2011).
67. Kaushik Sinha & Olivier de Weck. Structural Complexity Metric for Engineered Complex Systems and its Application. in *Proc. 14th Int. Depend. Struct. Model. Conf.* (2012).
68. Hatch, A. & Black, J. Electrospray Mission Modeling for CubeSats. (2013).